ACS AGRICULTURAL SCIENCE & TECHNOLOGY

pubs.acs.org/acsagscitech

Article

Synthetic Carbon Nanobionic Interfaces for Enhancement of Plant Photosynthetic Efficiency

Konstantinos T. Kotoulas, Thomas Hinton, Michael Zachariadis, George Kinman, Konstantinos Spyrou, James Hall, Robert H. Morris, Angela S. Kaloudi, Yunhong Jiang, Andrew D. Burrows, Gareth W. V. Cave, and Ming Xie*

Cite This: https://doi.org/10.1021/acsagscitech.5c01183

Read Online

ACCESS | Metrics & More | Article Recommendations | Supporting Information

ABSTRACT: Boosting the photosynthetic efficiency remains a critical challenge for sustainable crop productivity. In this study, the design, synthesis, and functional evaluation of two carbon-based nanomaterials are reported: a fluorescent carbon nanoassembly (Compound **1**) derived from citric acid and urea, and a cerium-incorporated variant (Compound **2**) incorporating redox-active cerium oxide domains. Comprehensive characterization confirmed the formation of nanostructured materials with tunable optical properties, surface functionalities, and crystalline features. Both compounds exhibited strong UV-A absorbance and blue photoluminescence, with Compound **2** showing enhanced emission and additional red-shifted features due to cerium integration. Greenhouse trials using *Raphanus sativus* as a model plant revealed significant improvements in biomass, pigment concentration, and ascorbic acid levels in the treated plants. Confocal microscopy and inductively coupled plasma mass spectrometry confirmed nanoparticle uptake and translocation, while flow cytometry revealed altered chloroplast fluorescence, supporting functional interaction at the organelle level. Together, these results establish carbon-based nanobionics as a promising platform for photonic enhancement of photosynthesis, offering new opportunities for advanced bioagricultural applications.

KEYWORDS: *carbon nanoassemblies, plant nanobionics, photosynthetic enhancement*

INTRODUCTION

Photosynthesis is a vital biological process that converts solar energy into chemical energy, enabling carbon fixation and oxygen production. While crop breeding has historically improved the grain-to-shoot mass ratio in plants, current research increasingly focuses on enhancing the efficiency of light energy capture and conversion to further improve biomass yield and meet global food demands.[1−3] Given the limitations of natural photosynthetic efficiency, estimated at 4.6% for C_3 and 6.0% for C_4 plants, strategies to augment light harvesting are being explored to address food security and support the UN's Zero Hunger Sustainable Development Goal.[4]

Inefficiency in photosynthesis lies in the limited utilization of the solar spectrum. Plants primarily absorb light in the blue and red regions, with green, UV, and far-red light largely underutilized or dissipated as heat through nonphotochemical quenching mechanisms.[5,6] Accessory pigments, such as carotenoids, expand the absorption range and provide photoprotection, yet even with these, only less than 43% of incident solar radiation is photosynthetically active.[7] UV radiation, which comprises 8% of solar energy, is typically harmful to plants, triggering oxidative stress and damage to chloroplasts, DNA, and membranes.[8]

To overcome these spectral limitations, novel photonic materials have been investigated to enhance light capture and energy transfer within plant systems. One promising approach involves the integration of carbon nanoassemblies (CNAs), fluorescent nanomaterials capable of converting unharvested UV and blue light into usable wavelengths within the photosynthetically active range.[8,9] CNAs are advantageous due to their low toxicity, biodegradability, photostability, and scalability from inexpensive precursors.[10−15] Their optical properties, including efficient fluorescence and potential Förster resonance energy or electron-transfer (FRET) capabilities, make them suitable candidates for augmenting the natural antenna complexes of photosystems I and II.

CNAs can be applied to plants via root uptake, foliar treatment, or seed priming.[16,17] Once internalized,[18,19] they can translocate through plant tissues via apoplastic and symplastic pathways,[20−23] potentially reaching chloroplasts where light harvesting occurs.[24] Studies have shown that such materials can improve photosynthetic efficiency, increase biomass,[25,26] and enhance nutrient uptake,[27−29] though these benefits are dose-dependent, with excessive concentrations leading to phytotoxic effects.[30]

The functional performance of CNAs can be further improved through metal doping, which enhances photoelectrical properties and introduces bioavailable micronutrients.[31] Cerium (Ce), although not essential for plant growth, is known to improve antioxidant enzyme activity, support membrane integrity, and

Received: December 23, 2025
Revised: March 9, 2026
Accepted: March 10, 2026

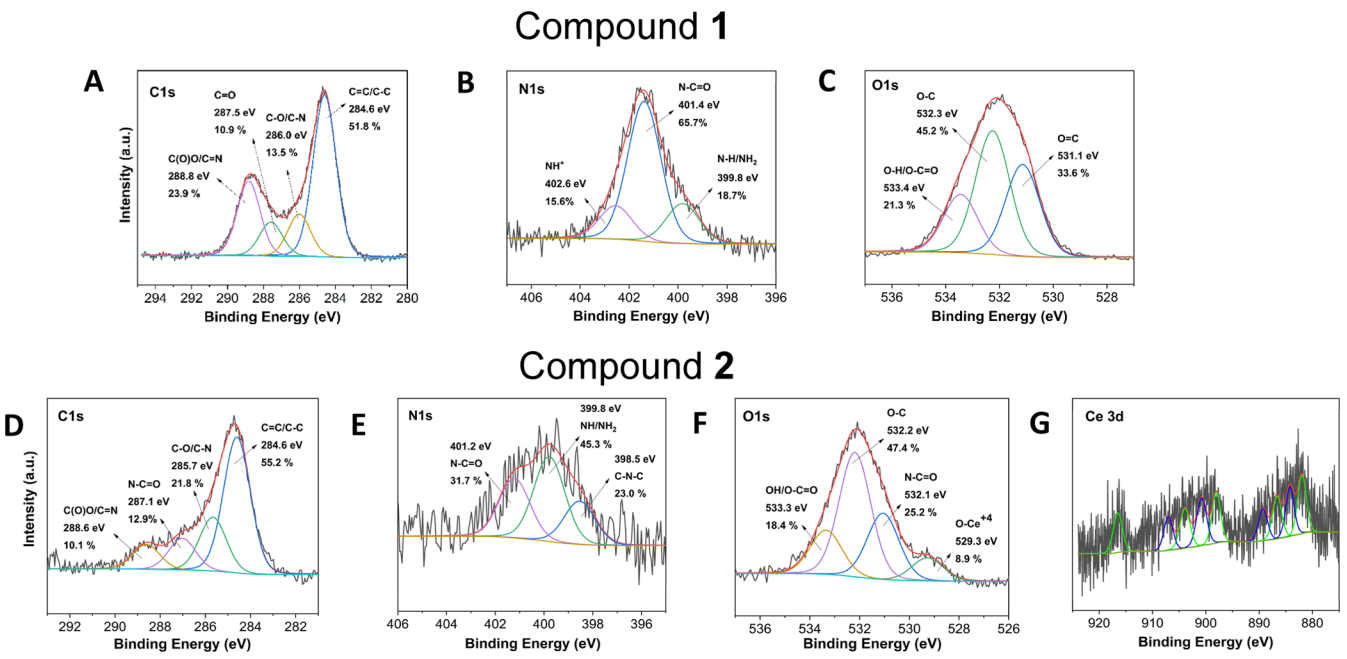

Figure 1. X-ray photoelectron spectroscopy (XPS) spectra of Compound 1: (a) High-resolution C 1s spectrum, (b) high-resolution N 1s spectrum, (c) high-resolution N 1s spectrum, high-resolution O 1s spectrum, and Compound 2: (d) high-resolution C 1s spectrum, showing increased carbonization and shifts indicative of coordination with cerium. (e) High-resolution N 1s spectrum, revealing nitrogen reconfiguration and the emergence of C−N−C (pyridinic) species (398.5 eV). (f) High-resolution O 1s spectrum, with a new peak corresponding to Ce−O bonds (529.3 eV). (g) High-resolution Ce 3d spectrum, confirming successful cerium doping and the presence of mixed Ce^{3+} and Ce^{4+} oxidation states. Atomic percentages for Compounds 1 and 2 are provided in Supporting Table S1.

promote photosynthesis at low concentrations.[32,33] When incorporated into carbon nanomaterials, cerium may synergistically amplify the effects of CNAs by increasing their energy transfer efficiency and ROS-scavenging capacity,[34,35] thereby supporting both light harvesting and photoprotection mechanisms. Recent studies further highlight that Ce-incorporated nanostructures display enhanced photoluminescence and introduce new emissive states arising from f−f electronic transitions,[36] making them particularly suitable for spectral conversion and photosynthesis augmentation.

This study investigates the synthesis and application of citric acid−urea-based carbon nanoassemblies, with and without cerium doping, as photonic nanomaterials for photosynthetic augmentation. CNAs are designed to convert excess UV and blue light into green and far-red light, thereby potentially enhancing the efficiency of the plant's native light-harvesting complex via fluorescence and hypothesized energy transfer mechanisms such as FRET or direct electron injection. We examine their effects on plant growth, chlorophyll production, and harvestable yield when applied through root uptake in greenhouse-grown crops.

MATERIALS AND METHODS

Synthesis and Characterization of the Nanomaterials

Two carbon nanoassemblies (CNAs) were synthesized via solvothermal methods. Compound **1** was derived from citric acid (5 mmol) and urea (5 mmol), in 10 mL H_2O treated at 210 °C and 10 bar for 5h. Compound **2** was synthesized by doping Compound **1** with cerium(III) nitrate hexahydrate using a microwave-assisted thermal process, followed by solvothermal treatment. Both compounds were purified via centrifugation and filtration, with Compound **1** undergoing further purification via column chromatography (Interchim puriFlash 5.125P).

Physicochemical properties were characterized using Fourier transform infrared spectroscopy (FTIR, Bruker INVENIO), X-ray photoelectron spectroscopy (XPS, SPECS GmbH), zeta potential, and powder X-ray diffraction (PXRD, STOE STADI P) to determine surface chemistry and crystallinity. Morphology and particle size were assessed via atomic force microscopy (AFM, Bruker Multimode 3D Nanoscope) and dynamic light scattering (DLS, ZSU3305). Thermal stability was evaluated by thermogravimetric analysis (TGA, Mettler Toledo TGA/SDTA851e), and optical properties were profiled using UV−visible and fluorescence spectroscopy (Agilent Cary 60, Agilent Cary Eclipse).

Plant Cultivation and Treatments

Raphanus sativus (Radish F1) seeds were germinated under dark, moist conditions for 3 days in 9 × 9 cm (0.5 L) square pots filled with 150 g of Levington M2 compost (N = 192, P = 98, K = 319 mg/L). Each experimental setup comprised 36 plants (18 treated, 18 control) grown in 100 × 55 cm garden trays connected to an Autopot passive watering system. After germination, plants were cultivated in a greenhouse for 32 days under controlled conditions (23 ± 10 °C, 176.64 ± 14.87 μmol m^{-2} s^{-1} light intensity, 16 h light/8 h dark photoperiod). In trial 1, treatments were administered weekly via either foliar or root infiltration using aqueous solutions of Compound **1** (100, 250, or 500 mg/L), while the control was treated with the equivalent concentrations of urea in water. In trial 2, Compound **1** was repeated at its optimal root infiltration concentration (250 mg/L), but the crops were only treated in the first 2 weeks. In addition to this, in trial 2, Compound **2** (100 mg/L) was trialled and was administered weakly via the root infiltration.

Throughout the trials, plant foliage area was monitored at different stages of the trial and quantified using ImageJ software. Post harvest, the crops were weighed and then lyophilized using a freeze dryer. These plant samples were dried under a vacuum (<5 Pa) at a condenser temperature of −71.8 °C.

Physiological and Biochemical Analysis

Internalization and translocation of the nanomaterials were verified using Confocal Airyscan super-resolution microscopy (Zeiss LSM 880) and inductively coupled plasma mass spectrometry (ICP-MS, PerkinElmer NexION 1000 ICP-MS). The functional impact on photosynthesis was assessed by quantifying chlorophyll and carotenoid

https://doi.org/10.1021/acsagscitech.5c01183
ACS Agric. Sci. Technol. XXXX, XXX, XXX−XXX

pigments via UV−vis spectroscopy and analyzing isolated chloroplasts using spectral flow cytometry.[37,38] Ascorbic acid levels were determined via high-performance liquid chromatography (HPLC, Agilent 1290 Infinity II). Untargeted metabolomic profiling of root and leaf tissues was conducted using hydrophilic interaction liquid chromatography linked to mass spectrometry (HILIC-MS) to identify metabolic shifts associated with treatment. Additionally, magnetic resonance imaging (MRI, 1.5T Siemens Avanto) was utilized to map T_2 relaxation properties and visualize internal root structure at high resolution.

Full experimental protocols, including synthesis parameters and instrumental settings, are provided in the Supporting Information.

RESULTS AND DISCUSSION

Two types of carbon nanoassemblies (CNAs) were synthesized via hydrothermal and microwave-assisted approaches: a citric acid−urea-based CNA (Compound **1**) and a cerium-incorporated variant (Compound **2**). The dark green coloration and aqueous dispersibility of the resulting materials suggested the successful formation of carbon nanomaterials.

Physicochemical and Structural Characterization of CNAs

X-ray photoelectron spectroscopy was used to assess the elemental composition and bonding environments of Compounds **1** and **2**, with a focus on carbon, oxygen, nitrogen, and cerium species (Figure 1).

The high-resolution C 1s spectrum of Compound **1** showed four main components (Figure 1a): sp^2/sp^3 hybridized C−C/C═C bonds at 284.6 eV (51.8%), C−O/C−N functionalities at 286.0 eV (13.5%), carbonyl groups (C═O) at 287.8 eV (10.9%), and carboxyl/amide groups (O−C═O/C═N) at 288.8 eV (23.9%). This distribution reflects a highly functionalized carbon surface, characteristic of citric acid and urea-derived carbon nanoassemblies. Upon cerium doping, the relative contributions of these components shifted markedly. The proportion of C−C and C═C increased to 55.2%, suggesting enhanced carbonization. The C−O/C−N contribution rose significantly to 21.8%, while the carboxyl/amide component was notably reduced to 10.1%. These changes, accompanied by a minor shift (0.2−0.4 eV) toward lower binding energies, indicate electrostatic interactions and possible coordination between cerium ions and oxygenated surface groups, consistent with a more graphitized carbon network and reduced surface oxidation.

In Compound **1**, the O 1s spectrum (Figure 1b) was dominated by signals from C═O groups at 531.1 eV (33.6%), C−O species at 532.3 eV (45.2%), and hydroxyl/carboxyl moieties at 533.4 eV (21.3%). These results support the presence of a hydrophilic, oxygen-rich surface.[39] In Compound **2**, cerium incorporation introduced a new low-energy peak at 529.3 eV (8.9%) corresponding to Ce−O bonds, confirming the chemical integration of cerium within the carbon framework. Concurrently, the carboxyl/hydroxyl component decreased to 18.4%, while the C−O and N−C═O signals remained prominent (47.4% and 25.2%, respectively). These observations suggest partial substitution or coordination of surface oxygenated groups with cerium, leading to a more stable composite structure.[39]

The N 1s spectrum of Compound **1** (Figure 1c) consisted mainly of amide nitrogen (N−C═O) at 401.4 eV (65.7%), along with contributions from NH/NH_2 groups at 399.8 eV (18.7%) and protonated nitrogen (NH^+) at 402.6 eV (15.6%). These functionalities originate from urea-derived precursors and are typical of hydrothermally synthesized nitrogen-doped carbon materials.[40] Compound **2** showed significant nitrogen reconfiguration. The amide peak decreased to 31.7%, while the NH/NH_2 content increased to 45.3%. Notably, a new peak emerged at 398.5 eV (23.0%), assigned to C−N−C (pyridinic) species,[41] indicating the formation of more aromatic nitrogen sites. These changes suggest that cerium doping promotes the conversion of amide groups into more stable nitrogen configurations, possibly via thermal dehydration and condensation processes during the secondary hydrothermal step. The Ce 3d spectrum of Compound 2 displayed the characteristic multiplet structure of cerium, confirming successful doping. Deconvolution revealed contributions from both Ce^{3+} and Ce^{4+} oxidation states in the 880−920 eV range, indicative of a mixed-valence system (Figure 1g). Specifically, the presence of Ce^{4+} was confirmed by prominent peaks at approximately 916.7 and 898.3 eV, alongside contributions from other characteristic Ce^{4+} satellites. The additional observation of peaks at lower binding energies, such as 880.5 and 884.9 eV within the $3d_5/_2$ doublet, confirmed the coexistence of Ce^{3+}.

The combined shifts in binding energy, reduction of carboxyl content, emergence of Ce−O and C−N−C species, and enhanced carbon backbone signal all support a mechanism in which cerium ions coordinate with oxygenated surface groups during hydrothermal synthesis. This coordination facilitates thermal reorganization, carbon condensation, and nitrogen transformation, resulting in a structurally integrated ceria-carbon composite rather than a simple physical mixture.

Atomic force microscopy (AFM) and dynamic light scattering (DLS) were employed to assess the morphology, particle size distribution, and colloidal stability of the carbon nanoassemblies.

AFM analysis of Compound **1** revealed well-dispersed, near-spherical nanostructures with average particle heights around 6 nm, consistent with the expected size range for individual carbon nanoassemblies formed via hydrothermal synthesis (Figure 2).

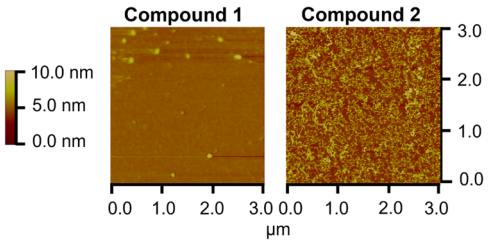

Figure 2. Atomic force microscopy (AFM) topography images of Compound **1** and Compound **2** deposited on a silicon wafer. Compound **1** displays well-dispersed, near-spherical nanostructures, while Compound **2** reveals a more aggregated network indicative of cerium acting as a bridging agent. Full section analysis is provided in Supporting Figures S1 and S2.

However, DLS measurements of the same material indicated a polydisperse system with three distinct hydrodynamic radii centered at approximately 5, 40, and 206 nm (Supporting Figure S3). The smallest population (5 nm) likely corresponds to discrete nanoparticles observed in the AFM, while the larger size distributions suggest the presence of loose aggregates or clustered assemblies in solution. The 40 and 206 nm populations may arise from weak interparticle interactions or hydrogen bonding among surface functional groups in aqueous media.

In contrast, Compound **2** exhibited a single dominant hydrodynamic radius of approximately 150 nm in DLS, indicative of a monodisperse population of uniformly sized

https://doi.org/10.1021/acsagscitech.5c01183
ACS Agric. Sci. Technol. XXXX, XXX, XXX−XXX

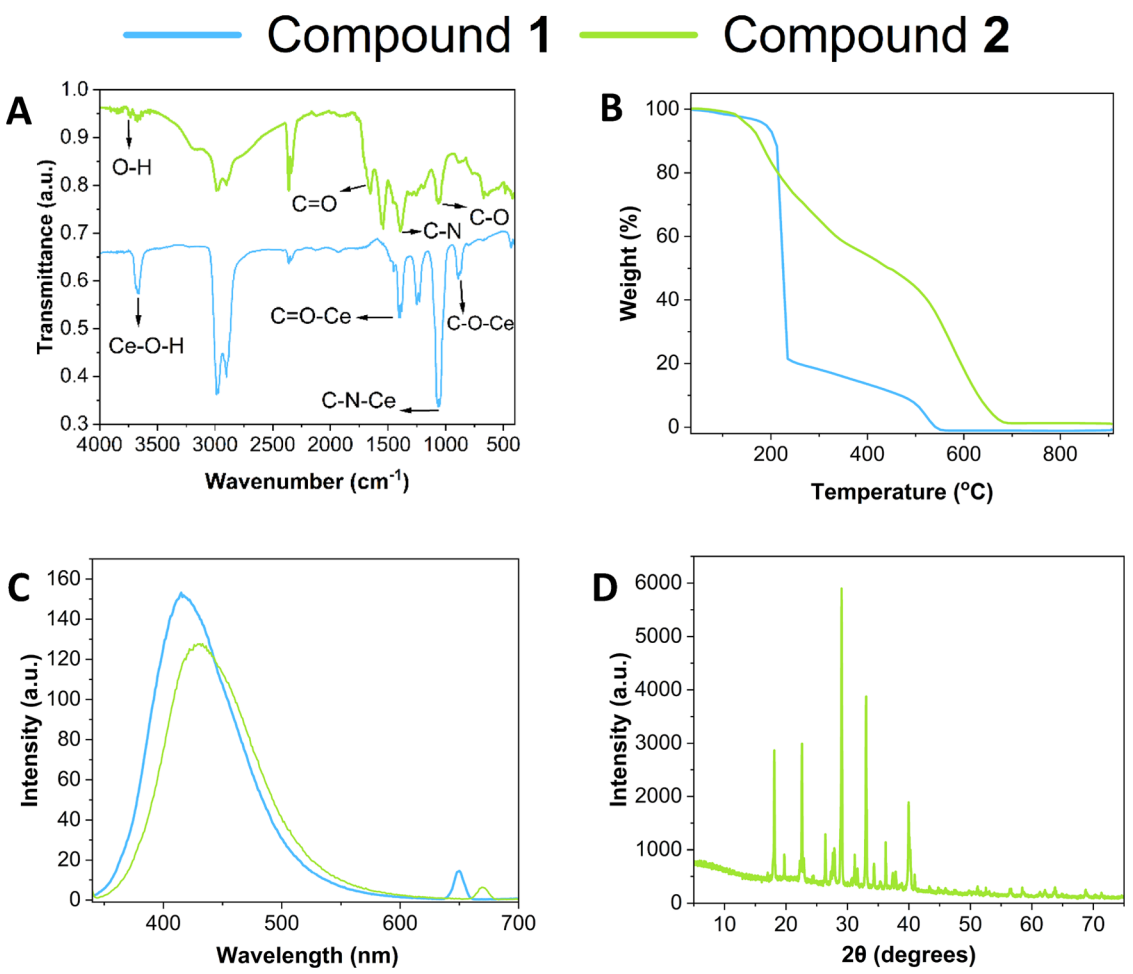

Figure 3. (A) Fourier transform infrared (FTIR) spectra of Compound **1** (blue) and Compound **2** (green), demonstrating the successful chemical modification of CNAs upon cerium doping. Shifts in peak positions and intensities indicate coordination between cerium ions and functional groups (O−H, N−H, C═O, C−O, C−N). (B) Thermogravimetric analysis (TGA) profiles of both compounds under a nitrogen atmosphere show enhanced thermal reactivity for the cerium-incorporated material. (C) Fluorescence emission spectra of Compound **1** (blue) and Compound **2** (green) in aqueous solutions (10 mg/L), excited at 330 nm. (D) Powder X-ray diffraction (PXRD) pattern of Compound **2**. Distinct peaks at 2θ values of 29.2°, 33.1°, 47.5°, 57.6°, and 59.0° can be assigned to CeO_2.[47].

aggregates (Supporting Figure S4). This shift toward larger, more uniform assemblies may be attributed to the presence of cerium ions, which can act as bridging or cross-linking agents between surface functional groups. The AFM images exhibit a network of organic matter with Ce active centers. The Ce catalyzes the carbon nanoassemblies and opens their structure, giving rise to formations like the one displayed in Figure 2. This hints at the role of cerium in facilitating carbon condensation and thermal reorganization.

Fourier transform infrared (FTIR) spectroscopy was used to examine the functional groups present in the CNAs and to assess the effect of cerium doping (Figure 3a). The spectra of Compound **1** and Compound **2** (cerium-incorporated), shown in black and red, respectively, revealed clear differences in both peak positions and intensities, indicating successful chemical modification upon doping.

Broad absorption bands in the 3200−3500 cm^{-1} range were observed in both compounds and are attributed to the O−H and N−H stretching vibrations. These peaks are indicative of surface hydroxyl and amine groups, commonly present in citric acid−urea-derived carbon nanoassemblies. Notably, Compound **2** exhibited sharper and more intense bands in this region, suggesting stronger or more numerous hydrogen-bonded functionalities or enhanced vibrational transitions due to coordination with cerium ions.[42,43] In the 1600−1750 cm^{-1} region, characteristic of C═O stretching in carbonyl and carboxyl groups, Compound **2** showed a shift to slightly lower wavenumbers alongside increased peak sharpness. This is consistent with coordination between the carbonyl oxygen atoms and cerium ions, which withdraw electron density and alter the vibrational energy of these bonds.[44] Additional peaks in the 1000−1300 cm^{-1} region, associated with C−O and C−N stretching modes, were also more pronounced in Compound **2**. These enhancements suggest that cerium interacts not only with carbonyl groups but also with amine or ether functionalities on the particle surface.[43] The cumulative effect of these changes, sharper peaks, increased intensity, and frequency shifts, supports the conclusion that cerium ions are coordinating to multiple functional groups within the CNA matrix.

Thermal stability and decomposition behavior of the carbon nanoassemblies were assessed by thermogravimetric analysis (TGA) under a nitrogen atmosphere. The TGA profiles for Compounds **1** and **2** exhibited distinct differences in their weight loss patterns, reflecting the impact of cerium incorporation on the thermal degradation process (Figure 3b). Compound **1** showed a gradual mass loss over a broad

https://doi.org/10.1021/acsagscitech.5c01183
ACS Agric. Sci. Technol. XXXX, XXX, XXX−XXX

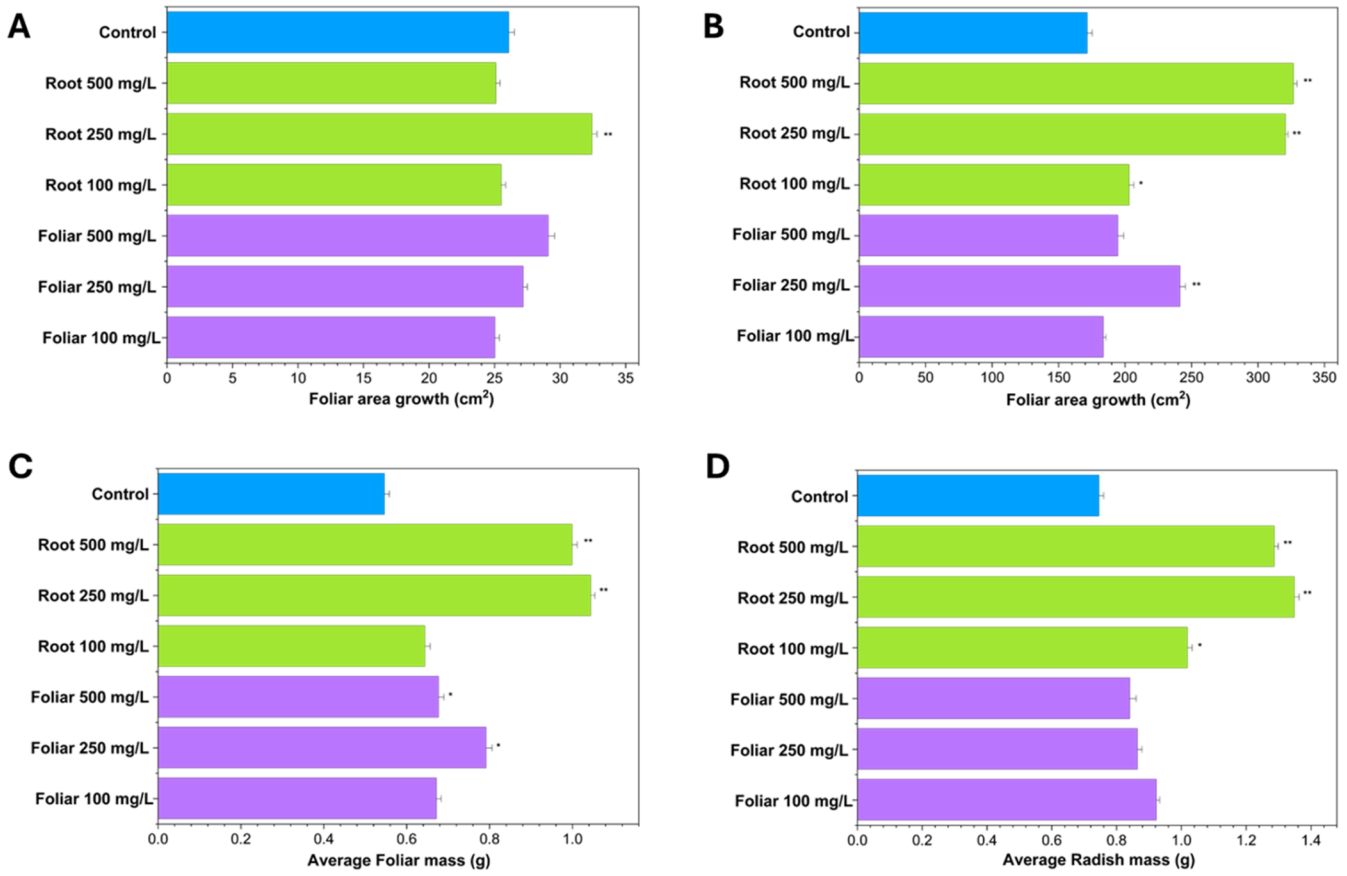

Figure 4. Column plots for trial 1 involving Compound **1** radish trials. The top row displays the foliar area growth (cm^2) during days 7−14 (A, Stage 1) and days 14-harvest (B, Stage 2). The bottom row displays the harvested *R. sativus* foliar (C) and radish (D) dry mass (g).

temperature range, indicative of a relatively stable organic matrix. This extended decomposition profile is characteristic of cross-linked structures formed through hydrothermal reactions between citric acid and urea, which degrade in multiple stages due to varied bond energies and functional group stability.[45] In contrast, Compound **2** exhibited a sharper and more pronounced weight loss event beginning near 200 °C. This behavior is attributed to the presence of cerium nitrate and its catalytic effect on the decomposition of the carbonaceous network. Cerium ions are known to lower the activation energy required for thermal degradation, thereby accelerating the breakdown of organic frameworks.[45] Moreover, cerium(III) nitrate itself decomposes at relatively low temperatures, releasing volatile species such as NOx and forming cerium oxide, which contributes to the observed mass loss.[46] The more abrupt decomposition in Compound **2** also suggests a higher content of labile oxygen-containing groups or structural irregularities introduced during the doping process. These features likely facilitate the early release of gaseous products and result in a more defined mass loss step. This trend supports the hypothesis that cerium doping alters the structural organization of the CNA, rendering it less thermally stable in the initial stages of degradation but potentially more reactive under light-driven or redox conditions.

The optical properties of the carbon nanoassemblies were investigated using UV−vis absorption and fluorescence spectroscopy. Among the chromatographically separated fractions of Compound **1** (Supporting Figure S5), Fractions 3 and 4 exhibited the strongest absorbance in the UV-A region (320−400 nm) and were therefore selected and combined for plant trials. Their efficient UV-A absorbance suggests a potential utility in light harvesting or photoprotection within the photosynthetically active spectrum. Both Compound **1** and Compound **2** exhibited blue fluorescence upon excitation at 330 nm, with primary emission peaks centered between 420−450 nm (Figure 3c), indicating that both share similar carbon-based emissive centers. Notably, Compound **2** showed a significantly higher fluorescence intensity, suggesting that cerium doping enhances the quantum yield or stabilizes emissive states. Additionally, Compound **2** displayed minor secondary emission peaks in the 600−700 nm region. These longer-wavelength emissions are absent or significantly weaker in Compound **1** and may originate from defect-related states, surface-bound cerium ions, or f−f transitions characteristic of cerium(III). These features broaden the emission profile and may enhance the energy transfer compatibility with plant photosystems.

Powder XRD analysis of Compound **2** revealed distinct diffraction peaks similar to cerium(IV) oxide nanoparticles (CeO_2), indicating that the cerium(III) nitrate precursor was fully converted and oxidized during hydrothermal synthesis. The absence of cerium(III) nitrate peaks and the emergence of sharp reflections at 2θ values of 29.2°, 33.1°, 47.5°, 57.6°, and 59.0° confirm the formation of crystalline CeO_2 with a fluorite-type structure[47] (Figure 3d). This transformation aligns with the TGA results, which showed a sharp weight loss at 200 °C, consistent with the cerium(III) nitrate decomposition and ceria formation. The sharpness of the CeO_2 peaks suggests relatively

https://doi.org/10.1021/acsagscitech.5c01183
ACS Agric. Sci. Technol. XXXX, XXX, XXX−XXX

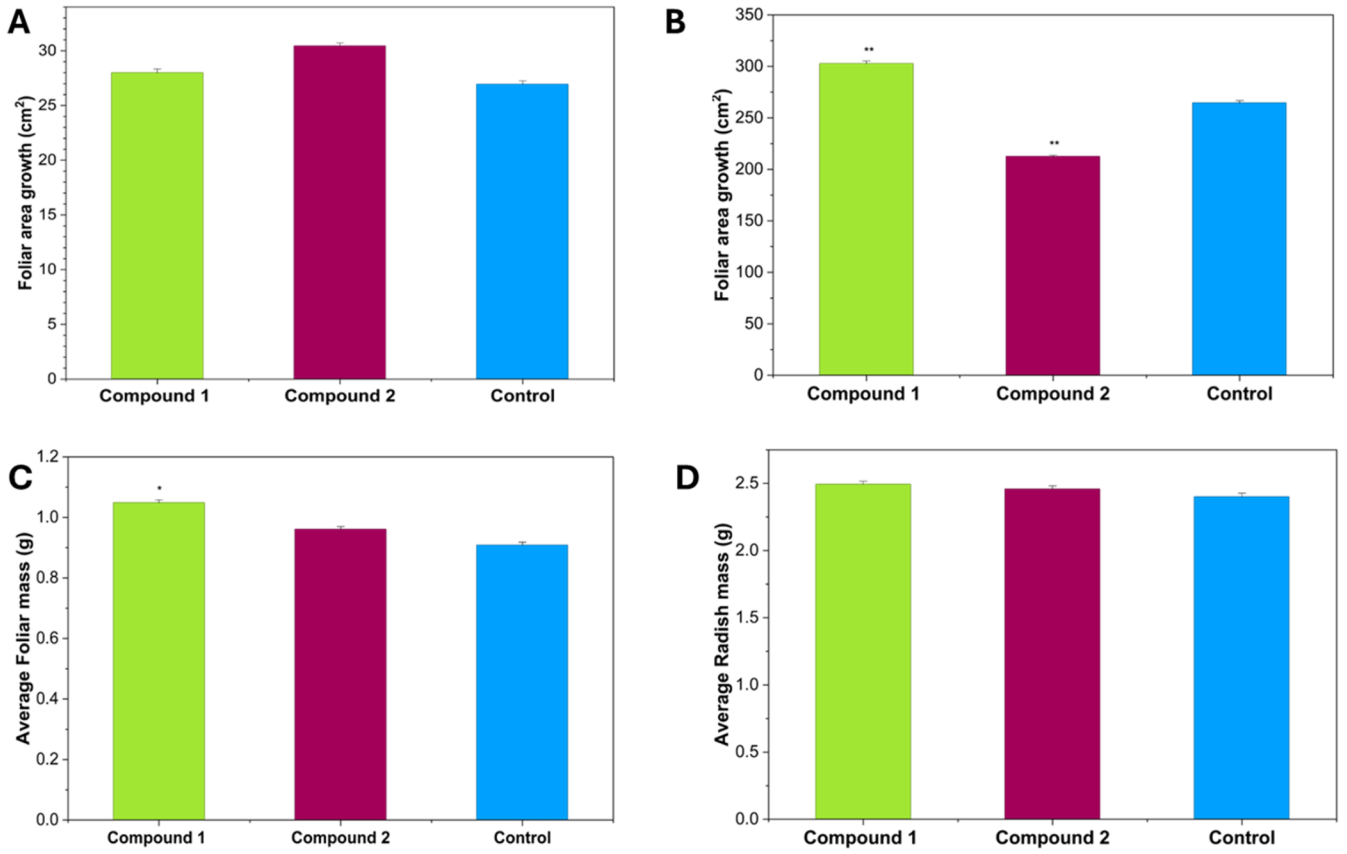

Figure 5. Column plots for trial 2 involving root treatments of Compound **1** (250 mg/L) and Compound **2** (100 mg/L). The top row displays the foliar area growth (cm^2) during days 7−14 (A, Stage 1) and days 14-harvest (B, Stage 2). The bottom row displays the harvested *R. sativus* foliar (C) and radish (D) dry mass (g). Values are presented as mean ± standard deviation of the mean (n = 18 plants per treatment). Statistical significance is indicated by $p^* < 0.05$ and $p^{**} < 0.005$. Foliar area measurements were performed via ImageJ (Supporting Figure S8).

well-ordered crystallites. However, their moderate breadth implies nanoscale dimensions, consistent with crystallite sizes governed by Scherrer broadening.[48] In contrast, Compound **1** displayed broad, diffuse features typical of amorphous or poorly crystalline carbonaceous materials, with no evidence of inorganic crystallinity (Supporting Figure S6). This amorphous character may arise from extensive polymerization and cross-linking of citric acid and urea precursors during the hydrothermal synthesis, resulting in a disordered carbon framework lacking long-range structural order (Supporting Figure S7). The PXRD pattern of Compound **2** shows both the amorphous carbon background and the superimposed crystalline cerium oxide reflections, indicating the successful formation of a hybrid nanocomposite. The carbon matrix, derived from citric acid and urea, likely influences the nucleation and dispersion of CeO_2 particles, creating a composite structure with both organic and inorganic domains. This dual-phase nature is consistent with the AFM analysis, which revealed a uniform nanoscale surface with discrete particle heights, and by XPS, which confirms the presence of Ce−O bonds and shifts in carbon and oxygen environments, indicative of strong interfacial coordination between the cerium oxide and the carbon framework. This structural evolution is also supported by the FTIR data, which revealed functional group shifts in Compound **2** suggestive of coordination between cerium ions and surface moieties (e.g., C═O, O−H). The presence of crystalline CeO_2 is significant, as it imparts thermal stability, redox activity, and catalytic potential to the nanocomposite, which would not be achieved if the nitrate precursor remained intact.

Growth and Physiological Assessment of CNA-Treated *Raphanus sativus*

The structural features characterized are particularly relevant for plant-based applications, as carbon nanomaterials have been shown to enhance photosynthesis through light conversion, and interaction with chloroplasts, forming a modified antenna pigment.[49−51] Cerium doping may further amplify these effects due to its known role in redox buffering and stimulation of stress-response pathways in the plant. To evaluate the functional potential of these nanomaterials in a biological context, greenhouse trials were conducted using F1 *R. sativus* (radish) as a model crop. The trials aimed to assess how CNA treatment, at different weekly dosages (100, 250, 500 mg/L) and application methods (foliar, root), can influence the radish growth and harvestable yield (trial 1). On the other hand, trial 2 trialled the optimum dosage of Compound **1** from the first trial and its cerium-incorporated alternative (Compound **2**) to monitor how it influences plant growth, pigment accumulation, vitamin levels, and harvestable yield.

In trial 1, *R. sativus* plants were treated with Compound **1** at concentrations of 100, 250, and 500 mg/L, applied via foliar spray[52] or root treatment.[53,54] These concentrations were selected due to concentrations between 100 and 500 mg/L being deemed as optimum, balancing activity and biosafety.[55] Plants that underwent root treatment with Compound **1** exhibited statistically significant increases in foliar area even

https://doi.org/10.1021/acsagscitech.5c01183
ACS Agric. Sci. Technol. XXXX, XXX, XXX−XXX

during Stage 1 (days 7−14), whereas foliar-treated crops showed no significant changes (Figure 4). While foliar application allows CNAs to penetrate leaves via stomata, cuticles, and wounds[56] and their small size facilitates passage through cell wall pores[52] root-treated crops exhibited superior leaf development consistent with similar findings reported in the literature.[25,57,58] Notably, root treatment at 500 mg/L and 250 mg/L led to highly significant increases in foliar area during Stage 2 of 91% and 87%, respectively, compared to the control ($p < 0.005$). Postharvest, the treated crops showed an increased harvestable yield under both treatment types (Figure 5), consistent with previous studies on CNAs in other crops, such as wheat.[59] However, the increases in the root-treated plants for 250 and 500 mg/L were again highly statistically significant for both the dry radish and foliar mass compared to the control (Figure 4).

Although Compound **1**-treated crops showed increased harvestable yields, they displayed lower concentrations of light-harvesting pigments (chlorophyll, carotenoids) per 100 mg of dry mass (Supporting Table S2). This apparent contradiction could be attributed to the proposed mechanisms by which CNAs enhance the photosynthetic efficiency. Specifically, it has been proposed that CNAs improve electron transport to the reaction center by absorbing UV and blue-green light.[50,60] This process is hypothesized to involve a donor−acceptor relationship between the CNA and chloroplasts,[61,62] leading to accelerated electron transfer.[63]

The result is typically enhanced light harvesting, ATP production, and oxygen evolution.[64−66] Therefore, the observed greater growth rates and yields, despite lower pigment levels, strongly suggest the formation of a novel, more efficient light-harvesting complex in the treated plants. Trial 1 identified the 250 mg/L root treatment as the optimum Compound **1** concentration, consistently yielding statistically significant increases in plant growth rates and overall harvestable yield, which aligns well with existing literature on CNA treatments.[67,25]

Values are presented as mean ± standard deviation of the mean (n = 18 plants per treatment). Statistical significance is indicated by $p^* < 0.05$ and $p^{**} < 0.005$. Foliar area measurements were performed via ImageJ (Supporting Figure S8).

The second trial utilized the Compound **1** (250 mg/L) optimum concentration, but the treatment was only utilized for the first 2 weeks, to see if the reduced treatment period would still improve the growth rates and yield. On the other hand, Compound **2** (100 mg/L) was administered weekly. Consistent with the first trial, Compound **1** resulted in increased foliar development across both growth stages, showing a highly statistically significant 14% increase in foliar area during Stage 2 (Figure 5), despite the treatment not being continued after the initial 2 weeks. In contrast, while Compound **2** initially produced a 13% increase in foliar development during Stage 1, the cerium- incorporated CNA exhibited significant detrimental effects on foliar area growth by the end of the trial. Specifically, a highly statistically significant 25% decrease in growth was observed during Stage 2 (Figure 5). This decline may suggest that excessive cerium dosage and/or prolonged treatment duration led to cytotoxic effects within the plants, potentially by inducing oxidative stress within the crops.[68] This was further evidenced by the dry crop masses from the compound **2** treatment, which, unlike Compound **1**, yielded no statistically significant improvements (Figure 5).

Analysis of pigment content revealed that compound **1** treatment yielded light-harvesting pigments (carotenoid, chlorophyll) comparable to the control, but improved ascorbic acid levels (Table 1). However, Compound **2** significantly

Table 1. Average Normalized Content of Carotenoids, Chlorophyll, and Ascorbic Acid in *R. sativus* Leaves following Compound 1 and Compound 2 Treatments in Trial 2[a]

treatment method	average carotenoid content (mg/L)	average chlorophyll content (mg/L)	average ascorbic acid content (mg/L)
Control	2.01 ± 0.73	10.21 ± 3.25	178 ± 73
Compound **1**	2.09 ± 0.40	10.35 ± 1.39	207 ± 34
Compound **2**	2.71 ± 0.47*	13.13 ± 2.65*	121 ± 22

[a]Values are presented as mean ± standard deviation ($n = 18$ plants per treatment). Statistical significance (where $n = 18$) is indicated by $p^* < 0.05$.

increased the carotenoid and chlorophyll concentrations by 35% and 29%, respectively (Table 1). This enhanced pigment generation by Compound **2** is consistent with cerium's reported antioxidant properties.[69,70]

In contrast, while compound **1** improved the ascorbic acid content by 16% per radish, compound **2** led to a statistically significant 47% reduction. This detrimental effect on ascorbic acid levels further reinforces the likelihood of excessive cerium dosage inducing cytotoxicity in treated plants, aligning with the previously noted hindrances on overall plant growth rate. The ascorbate depletion observed with Compound **2** likely reflects cerium-driven oxidative or metabolic stress, which is supported by the ICP-MS evidence of elevated Ce in roots of a subset of treated plants combined with limited foliar translocation, suggesting root-localized accumulation and systemic perturbation of antioxidant homeostasis. However, as ascorbic acid depletion serves only as an indirect indicator, direct toxicological evaluations are needed to confirm the precise nature and extent of this cytotoxicity.

The difference in the impact on plant growth of compounds **1** and **2** may also be attributed to their surface charge. Specifically, compound **1** has a more negative zeta potential of −18.08 mV, as opposed to the −1.50 mV of compound **2** (Supporting Figures S9 and S10). While plant root surfaces and cell walls generally carry a net negative charge due to components like pectin and cellulose,[71,72] potentially hindering the initial attachment and uptake of negatively charged nanomaterials through electrostatic repulsion, the situation changes once the nanoparticles enter the plant. If these nanomaterials overcome the initial root barrier and enter the vascular system, their surface charge can influence subsequent movement. The xylem vessels, responsible for upward transport, also possess negatively charged surfaces. In this context, Compound **1**'s more negative zeta potential could be beneficial, promoting dispersion and preventing aggregation or adhesion to xylem walls through electrostatic repulsion.[73] This mechanism could facilitate smoother and more efficient upward translocation through the xylem stream, allowing better distribution from the roots to the leaves. ICP-MS analysis provided additional evidence for the limited translocation of Compound **2**. While no cerium was detected in the leaves above the control threshold, cerium levels in 39% of the treated radishes were found to be 16-fold higher than the control (Supporting Table S3). This also links to the decrease in ascorbic acid levels observed with Compound **2**, which likely reflects cerium-driven oxidative or metabolic stress by elevated

https://doi.org/10.1021/acsagscitech.5c01183
ACS Agric. Sci. Technol. XXXX, XXX, XXX−XXX

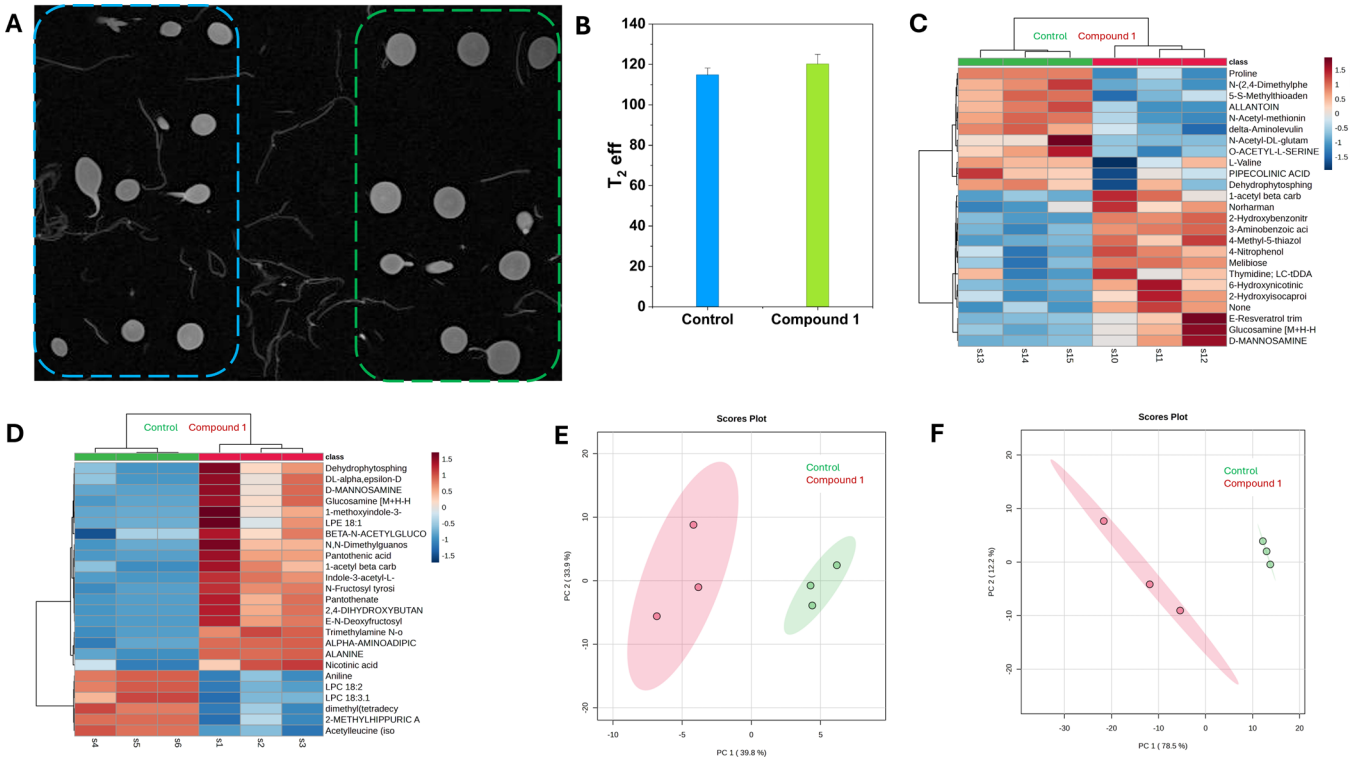

Figure 6. Proton density MRI scans (A) with the corresponding average T_2 relaxation time (B) for control and Compound **1** 250 mg/L treated groups (n = 8 per group). Normalized relative abundance heatmaps of leaves (C) and radishes (D) of the top 25 discriminants. PCA visualization of all 281 metabolites for leaf (E) and root (F) samples. Supervised analysis using partial least squares discriminant analysis (PLS-DA) can be found in Supporting Figure 12. The data set was visualized using MetaboAnalyst 6.[82].

Ce levels, suggesting root-localized accumulation and limited foliar translocation. These findings collectively reiterate that both the larger size and the more positive zeta potential of Compound **2** impede its uptake and transport to the plant canopy.

The characterization of Compounds **1** and **2** provides a framework for understanding their contrasting effects on plant performance. Surface analysis (FTIR, XPS) showed that cerium incorporation introduced new emissive states and enhanced blue photoluminescence, which could, in principle, improve spectral conversion. However, oxygen functional group analysis also revealed a reduction in carboxyl and amide moieties upon doping, suggesting fewer hydrophilic sites are available for biointeraction and uptake. Structural data (XRD, TGA) confirmed the formation of CeO_2 domains, but these crystalline features may have favored aggregation, as reflected in the monodisperse hydrodynamic radius (150 nm) of Compound **2** compared to the polydisperse distribution of smaller particles in Compound **1**. These differences likely influenced the internalization efficiency and translocation within the plant. Consistent with these findings, greenhouse trials showed stronger enhancements in crop yield and growth rate with Compound **1** treatments, indicating that the simpler carbon framework, with abundant surface functionalities and smaller particle fractions, was more effective in interacting with plant tissues and chloroplasts.

Imaging and Metabolomic Profiling of Compound 1 (Root-Treated) vs Control Crops. Metabolomic analysis was performed on the better-performing Compound **1** to link biochemical changes observed in crops to improvements in yield and growth rate. This analysis revealed treatment-specific shifts in both leaves and roots that align closely with the physiological enhancements reported in this study (Figure 6).

In the leaves, Compound **1**-treated crops exhibited a profile broadly similar to that of controls, with the exception of melibiose, which was strongly upregulated in treated plants but downregulated in the controls. Melibiose is a disaccharide implicated in carbon metabolism and osmoprotection in biological systems; its upregulation in CNA-treated leaves may indicate enhanced carbon flux and loading into the phloem, aligning with observed increases in foliar area (Figure 4) for compound 1-treated plants.[74] Furthermore, glucosamine and mannosamine were significantly upregulated in the treated crops, indicating the stimulation of the amino sugar pathway, which provides key precursors for cell wall polysaccharides and glycoproteins essential for tissue expansion and biomass accumulation. The increased resveratrol trimethyl ether may reflect the accumulation of antioxidant stilbene derivatives. Such compounds are known for radical scavenging and structural stability roles in other biological systems, and thus could contribute to improved redox balance under growth stress.[75] However, its precise biochemical role in radish root growth remains to be confirmed.

Glucosamine and mannosamine were concurrently upregulated in leaves and roots of CNA-treated plants, which may reflect an increased flux through the hexosamine biosynthesis pathway. This pathway generates UDP-N-acetylglucosamine, which is utilized in the glycosylation of proteins, glycolipids, and cell wall components in plants.[76] The concurrent upregulation of these metabolites across both tissues may reflect enhanced structural and metabolic remodeling processes, consistent with the increased foliar area and root biomass observed in treated

https://doi.org/10.1021/acsagscitech.5c01183
ACS Agric. Sci. Technol. XXXX, XXX, XXX−XXX

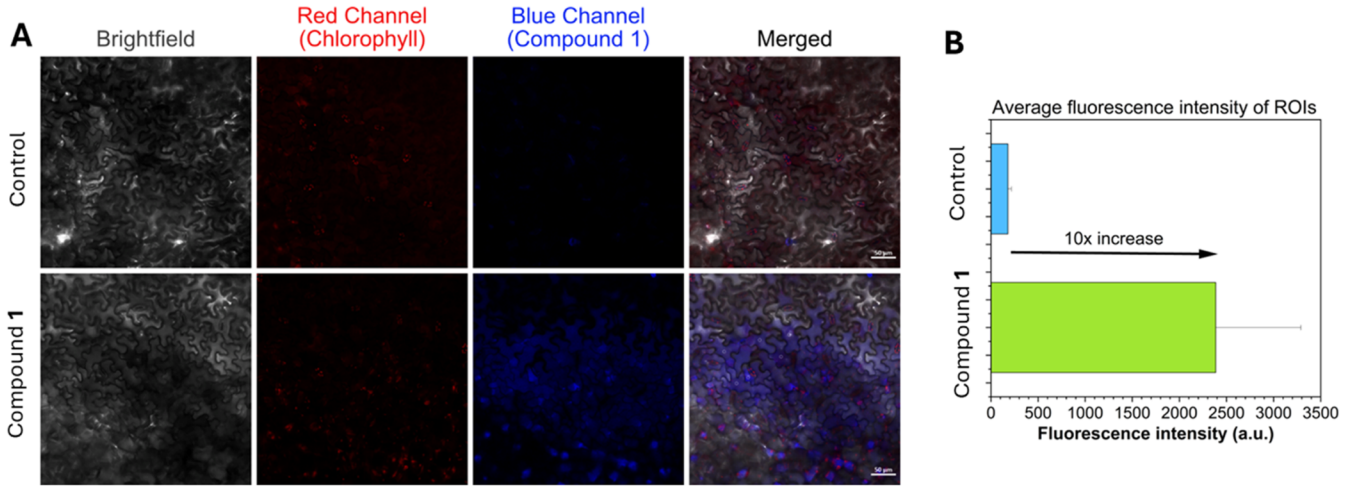

Figure 7. Confocal fluorescence microscopy imaging showing the localization of Compound **1** in *R. sativus* leaves (A). Small white circles on merged images denote regions of interest (ROI) displaying the increased fluorescence of Compound **1** compared to plant autofluorescence (B), with raw values presented in Supporting Figure S14.

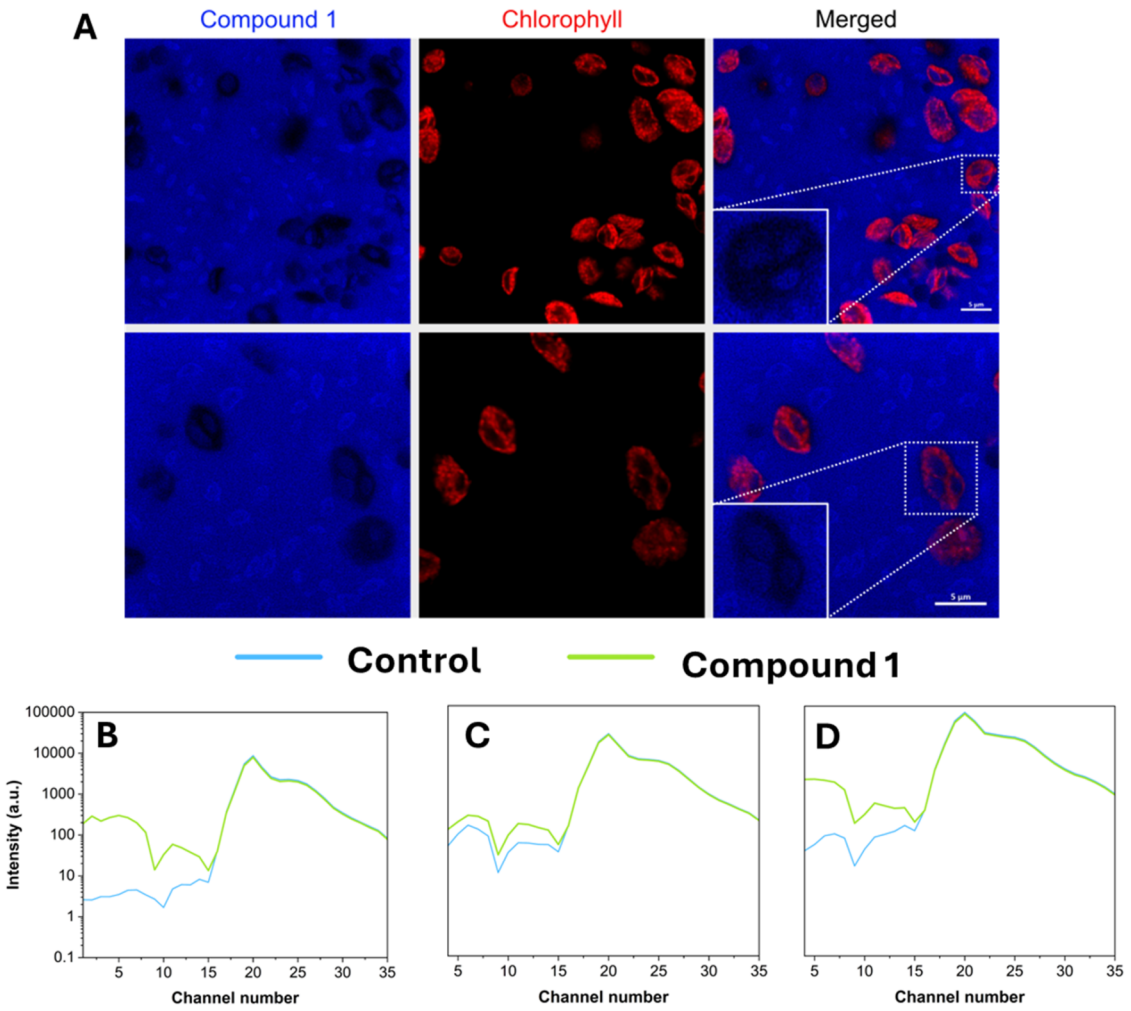

Figure 8. Confocal Airyscan microscopy images illustrating the distribution of blue fluorescent Compound **1** in *R. sativus* leaf cells (A). Control images, exhibiting no blue fluorescence under identical settings, are presented in Supporting Figure S15. Flow cytometry overlay (B, D) of fluorescence emission spectra for control and treated chloroplasts. Singlet chloroplasts (4−6 μm) were gated and analyzed across multiple emission channels after excitation at (B) 365 nm, (C) 405 nm, and (D) 488 nm. The gating strategy is shown in Supporting Figures S16 and S17.

plants, suggesting that CNA exposure could influence carbohydrate-amino-sugar metabolism pathways.

In the roots of CNA-treated plants, we also observed the upregulation of lysophosphatidylethanolamine (LPE), an

https://doi.org/10.1021/acsagscitech.5c01183
ACS Agric. Sci. Technol. XXXX, XXX, XXX−XXX

intermediate in phospholipid metabolism,[77] suggesting enhanced membrane synthesis,[78] which is important for cell expansion and root tissue growth.[79] In addition, elevated alanine and pantothenate levels point toward enhanced CoA biosynthesis and lipid metabolic activity, consistent with elevated energy and membrane demands during active growth.[80] Finally, modest increases in indole derivatives suggest potential modulation of tryptophan-dependent auxin biosynthesis, which is directly tied to root cell division and elongation.[81] Together, these shifts suggest possible mechanisms behind the improved growth rate and harvestable yield observed in Compound 1-treated crops (Figures 4 and 5).

MRI analysis was utilized to assess whether increased biomass observed in trial 2 was associated with altered tissue hydration or if it represented genuine structural growth. Specifically, MRI T_2 relaxation times are highly sensitive to water compartmentalization and mobility within plant tissues. The measurements showed no significant difference between Compound 1-treated (120.0 ± 4.8) and Control (114.0 ± 3.4) radishes. This lack of deviation is highly significant; it confirms that the internal tissue architecture and standard water retention capacities were preserved (Figure 6). Consequently, the larger crop sizes obtained via Compound **1** treatment are not the result of artificial hyperhydration or cellular swelling but rather represent proportional, healthy tissue development and genuine biomass accumulation.

Confocal Imaging and Flow Cytometry of CNA-Treated Plants and Chloroplasts

Due to the natural presence of compounds such as salicylic acid and ferulic acid in plant leaves and radishes, an inherent blue fluorescence is already evident in the plant tissue.[83] This endogenous fluorescence is particularly relevant, as it occurs in the same spectral region as the characteristic blue emissions of Compound **1** (Figure 7). Initial confocal imaging was performed on plants treated via syringe infiltration to address this (Figure 7). Despite the overlapping emissions, compound **1** displayed a 10-fold higher blue fluorescence intensity as opposed to the control (Figures 7, and S13). Compound **1**, under identical conditions, displayed greater blue fluorescence in the plant epidermis in both the blue and merged channels (Figure 7).

Although Compound **1** demonstrated significant beneficial effects on *R. sativus* growth and yield, the precise mechanisms at the subcellular level remain to be fully elucidated. To address this, *ex vivo* trials were undertaken, employing isolated chloroplasts to directly probe the interaction of Compound **1** with the photosynthetic apparatus. Following a 24 h incubation of isolated chloroplasts with Compound **1**, it was observed that the CNAs became embedded within the photosynthetic system, indicative of a newly formed modified light-harvesting system (Figure 8). To further probe the functional impact of CNA uptake on photosynthetic structures, flow cytometry was employed to analyze isolated chloroplasts from treated and control *R. sativus* samples. By screening only for singlets in the 4−6 μm size range, the technique ensured that the measurements reflected individual chloroplasts, eliminating aggregation effects. Spectral analysis revealed distinct shifts in fluorescence emission profiles between treated and untreated chloroplast populations (Figure 8). Treated chloroplasts (green trace) exhibited broader and elevated fluorescence intensity across multiple channels compared with the control (blue trace), suggesting an altered pigment environment. This change is attributed to the internalization of Compound **1**, which integrates into the photosynthetic apparatus, modifying local photophysical interactions. The enhanced emission in the 450−650 nm range aligns with the optical properties of the CNA, and supports the hypothesis that nanomaterial embedding modulates the pigment microenvironment, possibly through energy transfer or local light amplification. During the confocal measurements with 405 nm excitation, the blue fluorescence between 410 and 450 nm displayed a 10x increase in intensity (Figure 7), something also reflected via the 355, 405, and 488 nm excitation in the flow cytometry that displayed greater blue emissions during these excitations (Figure 8). This highlights that the new CNA-Chloroplast systems produce greater fluorescence from UV and blue light excitation. The increases in growth rates and crop yields seen during the plant trials may be a result of fluorescence-mediated energy transfer, the FRET mechanism, or direct electron injection. This is proposed as a working hypothesis supported by spectral overlap, enhanced photoluminescence, confocal localization, and altered chloroplast emission profiles. Direct quantification of energy or electron-transfer kinetics (for example, by time-resolved fluorescence) should be used in future studies to confirm and quantify the proposed mechanism, hence providing organellar-level evidence of photonic modulation by CNA uptake.

The flow cytometry and confocal imaging of Compound **1** show that, despite their negative surface charge, the nanomaterials were able to enter the chloroplasts, displaying distinct differences in emission profiles. The negative surface charge of the CNAs may help them overcome the electrostatic repulsion when entering the roots, aiding them in their translocation up the plant. This remains a working hypothesis, as a detailed mechanistic investigation into how CNAs overcome electrostatic barriers and are internalized in chloroplasts lies beyond the scope of the present study.

This study presents a comprehensive investigation into the synthesis, characterization, and functional evaluation of carbon-based nanobionics designed to augment plant photosynthesis. We report the formation of two distinct carbon nanoassemblies: a fluorescent citric acid/urea CNA (Compound **1**) and a cerium-incorporated variant (Compound **2**), both synthesized through hydrothermal methods. Detailed structural and spectroscopic analyses confirmed successful nanoparticle formation, with cerium incorporation altering surface chemistry, optical properties, and thermal behavior. Upon application to *Raphanus sativus* under greenhouse conditions, both compounds enhanced key physiological parameters, including biomass, chlorophyll content, and ascorbic acid levels. Confocal microscopy, ICP-MS, and flow cytometry provided direct evidence of nanoparticle uptake and chloroplast-scale interactions, supporting a mechanistic role in modulating light harvesting and internal energy transfer. These findings highlight the potential of carbon nanomaterials as functional light modulators in agricultural systems. By coupling spectral tuning with bioavailability and low toxicity, this platform opens promising avenues for nanotechnology-driven enhancement of crop performance in controlled environments and beyond. While visual comparisons of the harvested crops (Supporting Figure S18) highlight morphological changes under both treatments, the lack of statistically significant yield improvement and reduced ascorbic acid levels observed with Compound 2 indicate that its application requires finer tuning. Future studies must focus on optimizing the dosage of cerium-incorporated CNAs to harness their enhanced photoluminescent properties while strictly avoiding concentration-dependent cytotoxicity.

https://doi.org/10.1021/acsagscitech.5c01183
ACS Agric. Sci. Technol. XXXX, XXX, XXX−XXX

Crucially, to advance these nanomaterials toward real-world agricultural application and market readiness, rigorous toxicological profiling, such as direct reactive oxygen species (ROS) quantification, lipid peroxidation assays, and the evaluation of specific stress-response enzymes, must be performed to establish definitive biosafety thresholds. Furthermore, future work should focus on further elucidating the mechanistic basis of CNA−plant interactions. Time-resolved fluorescence spectroscopy could be employed to directly probe Förster resonance energy transfer processes between CNA emissive centers and chloroplast pigments, while absolute quantum yield measurements will be critical to quantitatively link the photophysical efficiency of these nanomaterials with their ability to modulate light for photosynthetic enhancement.

■ ASSOCIATED CONTENT

Supporting Information

The Supporting Information is available free of charge at https://pubs.acs.org/doi/10.1021/acsagscitech.5c01183.

Detailed experimental methodologies and materials, including synthesis protocols, advanced imaging and spectroscopic techniques (confocal microscopy, flow cytometry, FTIR, XPS, AFM, PXRD, DLS, UV−vis, TGA), elemental and biochemical assays (ICP-MS, HPLC, pigment/chloroplast extraction), metabolomic analysis, and MRI parameters. Supplementary results include atomic percentage data (Table S1), additional AFM topography and DLS size distributions (Figures S1−S4), UV−vis and PXRD spectra (Figures S5−S6), proposed synthesis mechanisms (Figure S7), ImageJ processing steps (Figure S8), extended physiological and elemental accumulation data (Tables S2−S4, Figures S9−S11), PLS-DA metabolomic plots (Figure S12), additional confocal imaging and flow cytometry gating strategies (Figures S13−S17), and comparative photographs of the harvested crops (Figure S18) (PDF)

■ AUTHOR INFORMATION

Corresponding Author

Ming Xie − *Department of Chemical Engineering, University of Bath, Bath BA2 7AY, U.K.;* orcid.org/0000-0003-2729-9746; Email: m.xie2@bath.ac.uk

Authors

Konstantinos T. Kotoulas − *Department of Chemical Engineering, University of Bath, Bath BA2 7AY, U.K.; Department of Chemistry, University of Bath, Bath BA2 7AY, U.K.; School of Science and Technology, Nottingham Trent University, Nottingham NG11 8NS, U.K.;* orcid.org/0000-0001-9070-2054

Thomas Hinton − *Department of Chemical Engineering, University of Bath, Bath BA2 7AY, U.K.*

Michael Zachariadis − *Core Research Facilities, Imaging Facility, University of Bath, Bath BA2 7AY, U.K.*

George Kinman − *Department of Chemical Engineering, University of Bath, Bath BA2 7AY, U.K.*

Konstantinos Spyrou − *Department of Materials Science and Engineering, University of Ioannina, Ioannina 45110, Greece;* orcid.org/0000-0002-2032-8439

James Hall − *School of Science and Technology, Nottingham Trent University, Nottingham NG11 8NS, U.K.*

Robert H. Morris − *School of Science and Technology, Nottingham Trent University, Nottingham NG11 8NS, U.K.;* orcid.org/0000-0001-5511-3457

Angela S. Kaloudi − *Department of Materials Science and Engineering, University of Ioannina, Ioannina 45110, Greece;* orcid.org/0009-0006-4052-0002

Yunhong Jiang − *Department of Applied Sciences, Northumbria University, Newcastle NE1 8ST, U.K.*

Andrew D. Burrows − *Department of Chemistry, University of Bath, Bath BA2 7AY, U.K.;* orcid.org/0000-0002-9268-4408

Gareth W. V. Cave − *School of Science and Technology, Nottingham Trent University, Nottingham NG11 8NS, U.K.;* orcid.org/0000-0002-4167-1332

Complete contact information is available at: https://pubs.acs.org/10.1021/acsagscitech.5c01183

Notes

The authors declare no competing financial interest.

■ ACKNOWLEDGMENTS

The authors thank the funding support by the Leverhulme Trust (RPG-2022-177). K.T.K thanks David Belton for his technical support and Jason Ralph-Smith (AutoPot UK)[84] for the collaboration. Financial support from the Royal Society of Chemistry (grant number C23-4364412079) is also gratefully acknowledged. The authors also acknowledge financial support from the Royal Society International Exchange (IEC\NSFC \242089).

■ REFERENCES

(1) Flügge, U.-I.; Westhoff, P.; Leister, D. Recent advances in understanding photosynthesis. *F1000Research* **2016**, *5*, No. 2890.

(2) Zelitch, I. The close relationship between net photosynthesis and crop yield. *BioScience* **1982**, *32*, 796−802.

(3) Long, S. P.; Marshall-Colon, A.; Zhu, X.-G. Meeting the global food demand of the future by engineering crop photosynthesis and yield potential. *Cell* **2015**, *161*, 56−66.

(4) Zhu, X.-G.; Long, S. P.; Ort, D. R. Improving photosynthetic efficiency for greater yield. *Annu. Rev. Plant Biol.* **2010**, *61*, 235−261.

(5) Cotton, C. A. R.; Douglass, J. S.; De Causmaecker, S.; Brinkert, K.; Cardona, T.; Fantuzzi, A.; Rutherford, A. W.; Murray, J. W. Photosynthetic constraints on fuel from microbes. *Front. Bioeng. Biotechnol.* **2015**, *3*, No. 36.

(6) Müller, P.; Li, X.-P.; Niyogi, K. K. Non-photochemical quenching. A response to excess light energy. *Plant Physiol.* **2001**, *125*, 1558−1566.

(7) Mancinelli, A. L. *Photomorphogenesis in Plants*, 2nd ed.; Springer Netherlands: Dordrecht, 1994; Vol. *10*, pp 211−269.

(8) Johnson, M. P. Photosynthesis. *Essays Biochem.* **2016**, *60*, 255−273.

(9) Cardona, T.; Shao, S.; Nixon, P. J. Enhancing photosynthesis in plants: the light reactions. *Essays Biochem.* **2018**, *62*, 85−94.

(10) Xu, X.; Ray, R.; Gu, Y.; Ploehn, H. J.; Gearheart, L.; Raker, K.; Scrivens, W. A. Electrophoretic analysis and purification of fluorescent single-walled carbon nanotube fragments. *J. Am. Chem. Soc.* **2004**, *126*, 12736−12737.

(11) Ding, C.; Zhu, A.; Tian, Y. Functional surface engineering of C-dots for fluorescent biosensing and in vivo bioimaging. *Acc. Chem. Res.* **2014**, *47*, 20−30.

(12) Wang, Y.; Hu, A. Carbon quantum dots: synthesis, properties and applications. *J. Mater. Chem. C* **2014**, *2*, 6921−6939.

(13) Zhang, X.; Jiang, M.; Niu, N.; Chen, Z.; Li, S.; Liu, S.; Li, J. Natural-Product-Derived Carbon Dots: From Natural Products to Functional Materials. *ChemSusChem* **2018**, *11*, 11−24.

(14) Zhang, J.; Yu, S.-H. Carbon dots: large-scale synthesis, sensing and bioimaging. *Mater. Today* **2016**, *19*, 382−393.
(15) Yang, S.; Sun, J.; Li, X.; Zhou, W.; Wang, Z.; He, P.; Ding, G.; Xie, X.; Kang, Z.; Jiang, M. Large-scale fabrication of heavy doped carbon quantum dots with tunable-photoluminescence and sensitive fluorescence detection. *J. Mater. Chem. A* **2014**, *2*, 8660−8667.
(16) Görlach, B. M.; Mühling, K. H. Phosphate foliar application increases biomass and P concentration in P deficient maize. *J. Plant Nutr. Soil Sci.* **2021**, *184*, 360−370.
(17) Badruzzaman, M.; Pinzon, J.; Oppenheimer, J.; Jacangelo, J. G. Sources of nutrients impacting surface waters in Florida: A review. *J. Environ. Manage.* **2012**, *109*, 80−92.
(18) Görlach, B. M.; Sagervanshi, A.; Henningsen, J. N.; Pitann, B.; Mühling, K. H. Uptake, subcellular distribution, and translocation of foliar-applied phosphorus: Short-term effects on ion relations in deficient young maize plants. *Plant Physiol. Biochem.* **2021**, *166*, 677−688.
(19) Li, W.; Zheng, Y.; Zhang, H.; Liu, Z.; Su, W.; Chen, S.; Liu, Y.; Zhuang, J.; Lei, B. Phytotoxicity, uptake, and translocation of fluorescent carbon dots in mung bean plants. *ACS Appl. Mater. Interfaces* **2016**, *8*, 19939−19945.
(20) Steudle, E. Water uptake by plant roots: an integration of views. *Plant Soil* **2000**, *226*, 45−56.
(21) Zarebanadkouki, M.; Trtik, P.; Hayat, F.; Carminati, A.; Kaestner, A. Root water uptake and its pathways across the root: quantifying water flow in the soil-root-plant system by neutron radiography and numerical modeling. *Sci. Rep.* **2019**, *9*, No. 13629.
(22) Kim, Y. X.; Ranathunge, K.; Lee, S.; Lee, Y.; Lee, D.; Sung, J. Composite transport model and water and solute transport across plant roots: an update. *Front. Plant Sci.* **2018**, *9*, No. 193.
(23) White, P. J. The pathways of calcium movement to the xylem. *J. Exp. Bot.* **2001**, *52*, 891−899.
(24) Li, H.; Huang, J.; Lu, F.; Liu, Y.; Song, Y.; Sun, Y.; Zhong, J.; Huang, H.; Wang, Y.; Li, S.; et al. Impacts of carbon dots on rice plants: boosting the growth and improving the disease resistance. *ACS Appl. Bio Mater.* **2018**, *1*, 663−672.
(25) Zhao, F.; Xin, X.; Cao, Y.; Su, D.; Ji, P.; Zhu, Z.; He, Z. Use of carbon dots to enhance plant growth and photosynthesis. *Nanomaterials* **2021**, *11*, No. 2717.
(26) Wang, C.; Ji, Y.; Cao, X.; Yue, L.; Chen, F.; Li, J.; Yang, H.; Wang, Z.; Xing, B. Carbon dots improve nitrogen bioavailability to promote the growth and nutritional quality of soybeans under drought stress. *ACS Nano* **2022**, *16*, 12415−12424.
(27) Zheng, Y.; Xie, G.; Zhang, X.; Chen, Z.; Cai, Y.; Yu, W.; Liu, H.; Shan, J.; Li, R.; Liu, Y.; Lei, B. Bioimaging application and growth-promoting behavior of carbon dots from pollen on hydroponically cultivated Rome lettuce. *ACS Omega* **2017**, *2*, 3958−3965.
(28) Waghmare, R. D.; Gore, A. H.; Anbhule, P. V.; Sohn, D.; Kolekar, G. B. Dataset on the shooting and rooting ability of Morus alba using waste tea residue derived carbon dots as an alternative of growth plant stimulator. *Data Brief* **2020**, *29*, No. 105345.
(29) Sciortino, A.; Cannizzo, A.; Messina, F. Carbon Nanodots: A Review—From the Current Understanding of the Fundamental Photophysics to the Full Control of the Optical Response. *C* **2018**, *4*, No. 67.
(30) Banerjee, P. P.; Pramanik, P.; Maity, A.; Maity, A.; Joshi, D. C.; Joshi, D.; Wani, S. H.; Wani, S.; Krishnan, P. Methods of Using Nanomaterials to Plant Systems and Their Delivery to Plants (Mode of Entry, Uptake, Translocation, Accumulation, Biotransformation and Barriers). *Adv. Phytonanotechnol.* **2019**, 123−152.
(31) Tummala, S.; Bandi, R.; Ho, Y.-P. Synthesis of Cu-doped carbon dot/chitosan film composite as a catalyst for the colorimetric detection of hydrogen peroxide and glucose. *Microchim. Acta* **2022**, *189*, No. 268.
(32) Li, X.; Fan, Y.; Ma, J.; Gao, X.; Wang, G.; Wu, S.; Liu, Y.; Yang, K.; Xu, E.; Pu, S.; Luo, A. Cerium improves the physiology and medicinal components of Dendrobium nobile Lindl. under copper stress. *J. Plant Physiol.* **2023**, *280*, No. 153896.
(33) Agathokleous, E.; Zhou, B.; Geng, C.; Xu, J.; Saitanis, C. J.; Feng, Z.; Tack, F. M.; Rinklebe, J. Mechanisms of cerium-induced stress in plants: A meta-analysis. *Sci. Total Environ.* **2022**, *852*, No. 158352.
(34) Kailashiya, J.; Dash, D. Nanoceria and its biomedical relevance. *Ann. Natl. Acad. Med. Sci.* **2019**, *55*, 14−17.
(35) Nguyen, T. L.; Phan, N. M.; Kim, J. Administration of ROS-Scavenging Cerium Oxide Nanoparticles Simply Mixed with Autoantigenic Peptides Induce Antigen-Specific Immune Tolerance against Autoimmune Encephalomyelitis. *ACS Appl. Mater. Interfaces* **2024**, *16*, 33106−33120.
(36) Li, J.; Guo, Z.; Liu, T.; Yu, F.; Zeng, J.; Zhang, Y.; Yin, L.; Liu, X.; Jiang, H.; Wang, X. Folic acid-modified cerium-doped carbon dots as photoluminescence sensors for cancer cells identification and Fe (III) detection. *Chemosensors* **2022**, *10*, No. 219.
(37) Pérez-Patricio, M.; Camas-Anzueto, J.; Sanchez-Alegría, A.; Aguilar-González, A.; Gutiérrez-Miceli, F.; Escobar-Gómez, E.; Voisin, Y.; Rios-Rojas, C.; Grajales-Coutiño, R. Optical method for the estimation of chlorophyll content in plant leaves. *Sensors* **2018**, *18*, No. 650.
(38) Li, Y.; Pan, X.; Xu, X.; Wu, Y.; Zhuang, J.; Zhang, X.; Zhang, H.; Lei, B.; Hu, C.; Liu, Y. Carbon dots as light converter for plant photosynthesis: Augmenting light coverage and quantum yield effect. *J. Hazard. Mater.* **2021**, *410*, No. 124534.
(39) Sun, X.-H.; Ma, M.; Tian, R.; Chai, H.-M.; Wang, J.-W.; Gao, L.-J. One-Pot Hydrothermal Method Preparation of Cerium−Nitrogen-Codoped Carbon Quantum Dots from Waste Longan Nucleus as a Fluorescent Sensor for Sensing Drug Rifampicin. *ACS Omega* **2023**, *8*, 34859−34867.
(40) Stachowska, J. D.; Murphy, A.; Mellor, C.; Fernandes, D.; Gibbons, E. N.; Krysmann, M. J.; Kelarakis, A.; Burgaz, E.; Moore, J.; Yeates, S. G. A rich gallery of carbon dots based photoluminescent suspensions and powders derived by citric acid/urea. *Sci. Rep.* **2021**, *11*, No. 10554.
(41) Lazar, P.; Mach, R.; Otyepka, M. Spectroscopic fingerprints of graphitic, pyrrolic, pyridinic, and chemisorbed nitrogen in N-doped graphene. *J. Phys. Chem. C* **2019**, *123*, 10695−10702.
(42) Hafez, N. A.; Fadl, E.; Ebrahim, S.; Soliman, M.; Shokry, A. Fluorescent cerium doped carbon quantum dots for detection of ferric ions. *Ceram. Int.* **2025**, *51*, 34350−34364.
(43) Shen, C.-H.; Chuang, C.-T.; Gu, Y.; Ho, W. H.; Song, Y.; Chen, Y. C.; Wang, Y.; Kung, C. W. Cerium-based metal−organic framework nanocrystals interconnected by carbon nanotubes for boosting electrochemical capacitor performance. *ACS Appl. Mater. Interfaces* **2021**, *13*, 16418−16426.
(44) Du, J.; Qi, S.; Chen, J.; Yang, Y.; Fan, T.; Zhang, P.; Zhuo, S.; Zhu, C. Fabrication of highly active phosphatase-like fluorescent cerium-doped carbon dots for in situ monitoring the hydrolysis of phosphate diesters. *RSC Adv.* **2020**, *10*, 41551−41559.
(45) Strauss, V.; Wang, H.; Delacroix, S.; Ledendecker, M.; Wessig, P. Carbon nanodots revised: the thermal citric acid/urea reaction. *Chem. Sci.* **2020**, *11*, 8256−8266.
(46) Shabani, S.; Jamalpour, M.; Mirkazemi, S. M.; Trasatti, S. Low-concentration Ce-based dopants for high thermal stability in mesoporous γ-Al2O3 beads. *Ceram. Int.* **2025**, *51*, 25508−25519.
(47) Grivel, J.-C.; Guevara, M. J. S.; Zhao, Y.; Tang, X.; Pallewatta, P. G. A. P.; Bednarčík, J.; Watenphul, A. Thermal behavior and decomposition of cerium (III) butanoate, pentanoate and hexanoate salts upon heating in argon. *J. Anal. Appl. Pyrolysis* **2017**, *126*, 77−87.
(48) Camacho-Rios, M. L.; Herrera-Pérez, G.; RuizEsparza-Rodriguez, M.; Lardizabal-Gutierrez, D.; García-Mireles, E.; Ramirez-Valdespino, C. Microstructural Effects of Cerium Oxide Nanoparticles Obtained by the Hydrothermal Route: HRTEM and XRD Analysis. *Microsc. Microanal.* **2024**, *30*, 2135−2136.
(49) Holder, C. F.; Schaak, R. E. Tutorial on powder X-ray diffraction for characterizing nanoscale materials. *ACS Nano* **2019**, *13*, 7359−7365.
(50) Nabiev, I.; Rakovich, A.; Sukhanova, A.; Lukashev, E.; Zagidullin, V.; Pachenko, V.; Rakovich, Y. P.; Donegan, J. F.; Rubin, A. B.; Govorov, A. O. Fluorescent quantum dots as artificial antennas for

https://doi.org/10.1021/acsagscitech.5c01183
ACS Agric. Sci. Technol. XXXX, XXX, XXX−XXX

enhanced light harvesting and energy transfer to photosynthetic reaction centers. *Angew. Chem., Int. Ed.* **2010**, *49*, 7217−7221.
(51) Zhang, M.; Hu, L.; Wang, H.; Song, Y.; Liu, Y.; Li, H.; Shao, M.; Huang, H.; Kang, Z. One-step hydrothermal synthesis of chiral carbon dots and their effects on mung bean plant growth. *Nanoscale* **2018**, *10*, 12734−12742.
(52) Wang, H.; Zhang, M.; Song, Y.; Li, H.; Huang, H.; Shao, M.; Liu, Y.; Kang, Z. Carbon dots promote the growth and photosynthesis of mung bean plants. *Carbon* **2018**, *136*, 94−102.
(53) Li, H.; Huang, J.; Lu, F.; Liu, Y.; Song, Y.; Sun, Y.; Zhong, J.; Huang, H.; Wang, Y.; Li, S.; et al. Impacts of carbon dots on rice plants: boosting the growth and improving the disease resistance. *ACS Appl. Bio Mater.* **2018**, *1*, 663−672.
(54) Abdel-Aziz, H. M. M.; Hasaneen, M. N. A.; Omer, A. M. Impact of engineered nanomaterials either alone or loaded with NPK on growth and productivity of French bean plants: Seed priming vs foliar application. *S. Afr. J. Bot.* **2019**, *125*, 102−108.
(55) Abinaya, K.; Raja, K.; Moorthy, P. S.; Senthil, A.; Chandrakumar, K.; Raja, K. Impact of green carbon dot nanoparticles on seedling emergence, crop growth and seed yield in blackgram. *Sci. Rep.* **2024**, *14*, No. 23783.
(56) Li, G.; Xu, J.; Xu, K. Physiological Functions of Carbon Dots and Their Applications in Agriculture: A Review. *Nanomaterials* **2023**, *13*, No. 2684.
(57) Li, H.; Huang, J.; Liu, Y.; Lu, F.; Zhong, J.; Wang, Y.; Li, S.; Lifshitz, Y.; Lee, S.-T.; Kang, Z. Impacts of Carbon Dots on Rice Plants: Boosting the Growth and Improving the Disease Resistanc. *Nano Res.* **2018**, *1*, 663−672.
(58) Ali, S.; Mehmood, A.; Khan, N. Uptake, Translocation, and Consequences of Nanomaterials on Plant Growth and Stress Adaptation. *J. Nanomater.* **2021**, *2021*, No. 6677616.
(59) Görlach, B. M.; Amit, S.; Henningsen, J. N.; Pitann, B.; Mühling, K. H. Uptake, Subcellular Distribution, and Translocation of Foliar-Applied Phosphorus: Short-Term Effects on Ion Relations in Deficient Young Maize Plants. *Plant Physiol. Biochem.* **2021**, *166*, 677−688.
(60) Gong, Y.; Dong, Z. Transfer, transportation, and accumulation of cerium-doped carbon quantum dots: Promoting growth and development in wheat. *Ecotoxicol. Environ. Saf.* **2021**, *226*, No. 112852.
(61) Zhang, M.; Hu, L.; Wang, H.; Song, Y.; Liu, Y.; Li, H.; Shao, M.; Huang, H.; Kang, Z. One-step hydrothermal synthesis of chiral carbon dots and their effects on mung bean plant growth. *Nanoscale* **2018**, *10*, 12734−12742.
(62) Chandra, S.; Pradhan, S.; Mitra, S.; Patra, P.; Bhattacharya, A.; Pramanik, P.; Goswami, A. High throughput electron transfer from carbon dots to chloroplast: a rationale of enhanced photosynthesis. *Nanoscale* **2014**, *6*, 3647−3655.
(63) Tan, T. L.; Zulkifli, N. A.; Zaman, A. S. K.; Jusoh, Mb.; Yaapar, M. N.; Rashid, S. A. Impact of photoluminescent carbon quantum dots on photosynthesis efficiency of rice and corn crops. *Plant Physiol. Biochem.* **2021**, *162*, 737−751.
(64) Wang, H.; Zhang, M.; Song, Y.; Li, H.; Huang, H.; Shao, M.; Liu, Y.; Kang, Z. Carbon dots promote the growth and photosynthesis of mung bean plants. *Carbon* **2018**, *136*, 94−102.
(65) Alas, M. O.; Genc, R. An investigation into the role of macromolecules of different polarity as passivating agent on the physical, chemical and structural properties of fluorescent carbon nanodots. *J. Nanopart. Res.* **2017**, *19*, No. 185.
(66) Wu, M. J.; Hu, H.-H.; Siao, C.-Z.; Liao, Y.-M.; Chen, J.-H.; Li, M.-Y.; Lin, T.-Y.; Chen, Y.-F. All organic label-like copper (II) ions fluorescent film sensors with high sensitivity and stretchability. *ACS Sens.* **2018**, *3*, 99−105.
(67) do Nascimento, C. W. A.; Marques, M. C. Metabolic alterations and X-ray chlorophyll fluorescence for the early detection of lead stress in castor bean (*Ricinus communis*) plants. *Acta Sci., Agron.* **2018**, *40*, No. e39392.
(68) A/P Chowmasundaram, Y.; Tan, T. L.; Nulit, R.; Jusoh, M.; Rashid, S. A. Recent developments, applications and challenges for carbon quantum dots as a photosynthesis enhancer in agriculture. *RSC Adv.* **2023**, *13*, 25093−25117.
(69) Ayub, M. A.; Ahmad, M.; Rico, H. R.; Abbasi, C. M.; Umar, G. H.; Wright, W.; Nadeem, A. L.; Fox, M.; Rossi, J. P. L. Divergent effects of cerium oxide nanoparticles alone and in combination with cadmium on nutrient acquisition and the growth of maize (*Zea mays*). *Front. Plant Sci.* **2023**, *14*, No. 1151786.
(70) Ahmad, S.; Sehrish, A. K.; Ai, F.; Zong, X.; Alomrani, S. O.; Al-Ghanim, K. A.; Alshehri, M. A.; Ali, S.; Guo, H. Morphophysiological, biochemical, and nutrient response of spinach (Spinacia oleracea L.) by foliar CeO2 nanoparticles under elevated CO_2. *Sci. Rep.* **2024**, *14*, No. 25361.
(71) Morshedloo, M. R.; Jabbari, N.; Azizi, M.; Nazari, M.; Zahedi, S. M.; Viapiana, A. Enhancing salt tolerance in Mentha × gracilis through foliar applications of titanium and nano-titanium. *BMC Plant Biol.* **2025**, *25*, 1088.
(72) Lodish, H.; Berk, A.; Zipursky, S. L.; Matsudaira, P.; Baltimore, D.; Darnell, J. *Molecular Cell Biology*, 4th ed.; W.H.Freeman & Co Ltd: New York, 2000.
(73) Alnaddaf, L. M.; Al-Khayri, J. M.; Jain, S. M. Nanomaterial Interactions With Plant Cellular Mechanisms. In *Nanomaterial Interactions with Plant Cellular Mechanisms and Macromolecules and Agricultural Implications*; Springer: Switzerland, 2022; Vol. *1*, pp 341−358.
(74) Lemoine, R.; La Camera, S.; Atanassova, R.; Dédaldéchamp, F.; Allario, T.; Pourtau, N.; Bonnemain, J.-L.; Laloi, M.; Coutos-Thévenot, P.; Maurousset, L.; et al. Source-to-sink transport of sugar and regulation by environmental factors. *Front. Plant Sci.* **2013**, *4*, No. 272.
(75) Zielińska-Przyjemska, M.; Ignatowicz, E.; Krajka-Kuźniak, V.; Baer-Dubowska, W. Effect of tannic acid, resveratrol and its derivatives, on oxidative damage and apoptosis in human neutrophils. *Food Chem. Toxicol.* **2015**, *84*, 37−46.
(76) Chen, Y.-H.; Cheng, W.-H. Hexosamine biosynthesis pathway in plants. *Front. Plant Sci.* **2024**, *15*, No. 1349064.
(77) Chen, X.; Snyder, C. L.; Truksa, M.; Shah, S.; Weselake, R. J. sn-Glycerol-3-phosphate acyltransferases in plants. *Plant Signaling Behav.* **2011**, *6*, 1695−1699.
(78) Völz, R.; Park, J.-Y.; Harris, W.; Hwang, S.; Lee, Y.-H. Lyso-phosphatidylethanolamine primes the plant immune system and promotes basal resistance against hemibiotrophic pathogens. *BMC Biotechnol.* **2021**, *21*, No. 7.
(79) Lavell, A. A.; Benning, C. Cellular organization and regulation of plant glycerolipid metabolism. *Plant Cell Physiol.* **2019**, *60*, 1176−1183.
(80) Parthasarathy, A.; Savka, M. A.; Hudson, A. O. The synthesis and role of β-alanine in plants. *Front. Plant Sci.* **2019**, *10*, No. 921.
(81) Zhao, Y. Auxin biosynthesis and its role in plant development. *Annu. Rev. Plant Biol.* **2010**, *61*, 49−64.
(82) MetaboAnalyst. https://www.metaboanalyst.ca/. (accessed October 2025).
(83) Lichtenthaler, H. K.; Schweiger, J. Cell wall bound ferulic acid, the major substance of the blue fluorescence emission of plants. *J. Plant Physiol.* **1998**, *152*, 272−282.
(84) AutoPot Watering Systems UK. Power Free, Indoor & Outdoor Irrigation | AutoPot Watering Systems UK. https://autopot.co.uk/. (accessed July 2025).

https://doi.org/10.1021/acsagscitech.5c01183
ACS Agric. Sci. Technol. XXXX, XXX, XXX−XXX